JOURNAL OF SYNCHROTRON RADIATION

ISSN 1600-5775

Direct cross-sectional imaging using X-ray Compton scattering: application to commercial batteries

Naruki Tsuji, Kentaro Kajiwara, Masayoshi Itou and Yoshiharu Sakurai*

JASRI/SPring-8, 1-1-1 Kouto, Sayo, Hyogo 679-5198, Japan. *Correspondence e-mail: sakurai@spring8.or.jp

Received 26 April 2021
Accepted 8 June 2021

Edited by A. Momose, Tohoku University, Japan

Keywords: Compton scattering; synchrotron X-ray imaging; lithium battery.

A synchrotron-based technique using Compton scattering imaging is presented. This technique has been applied to a coin battery (CR2023), and the cross-sectional image has been obtained in 34 ms without sample rotation. A three-dimensional image of the whole structure has been reconstructed from 74 cross-sectional images taken consecutively by scanning the incident, wide X-ray beam along one direction. This work demonstrates that quick cross-sectional imaging of regions of interest and three-dimensional image reconstruction without sample rotation are feasible using Compton scattering imaging.

1. Introduction

X-ray Compton scattering is one of the most promising probes for non-destructive imaging of the internal structure and material behavior of objects as it employs high-energy X-rays greater than 100 keV (Guzzardi & Licitra, 1988; Harding & Harding, 2010; Margret *et al.*, 2015; Boldo & Appoloni, 2014). Compton scattering imaging (CSI) at a back-scattering geometry is known as back scattered imaging, and is used in the baggage screening systems at airports. Portable imaging devices have recently been developed and used in the security sector to find hazardous materials and drugs (Harding & Harding, 2010). The advantage of CSI is its high sensitivity to light-element materials, such as organic matter, since Compton scattering dominates the electron–photon interactions for light elements at high energies. Another advantage is that, by employing well defined X-ray beams, CSI allows direct access to a cross-sectional image of an object without object rotation. Hence, synchrotron-based CSI has been developed to visualize the internal structures and material behaviors in lithium-ion batteries (Itou *et al.*, 2015; Suzuki *et al.*, 2016, 2017).

CSI techniques are categorized into three types based on the geometry of experimental setups, which include point-by-point, line-by-line and plane-by-plane. In the point-by-point type, a single-element detector is arranged to detect scattered X-rays through a collimator focused on one point of a sample. This type of CSI has been employed to investigate lithium-ion batteries at BL08W, SPring-8 (Sakurai, 1998). The CSI setup at BL08W is equipped with a nine-segment Ge solid-state detector (SSD) placed at a scattering angle of about 90°. The nine pairs of a Ge-SSD segment and a collimating slit focus on a single probing volume inside the sample. The advantageous feature of this setup is that one can measure the line shape of Compton scattered X-rays as well as their intensity since the Ge-SSD has a sufficient energy resolution. For this setup, an analytical method, so-called the S-parameter analysis, has been developed, which normalizes the central area of line shape by its tail area (Suzuki *et al.*, 2016). After calibration,

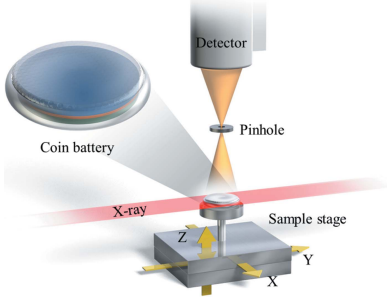

the digitized value (*i.e.* S-parameter) represents the lithium concentration of electrode materials. The S-parameter analysis has been used to reveal the change of lithium distribution in working batteries (Itou *et al.*, 2015; Suzuki *et al.*, 2016, 2017).

2. Experimental setup

CSI measurements were carried out with white X-rays at BL28B2, SPring-8 (Chikaura *et al.*, 2001). Fig. 1 shows the photon flux as a function of energy at BL28B2 and the photon flux with absorption correction by Sn with 1 mm thickness. The photon flux was simulated by *SPECTRA* (Tanaka & Kitamura, 2001). Since the Sn film with 1 mm thickness can absorb almost all the low-energy X-rays below 50 keV, the Sn film is adopted as an attenuator to cut this region of white X-rays from the bending magnets. Note that there is no filter for scattered X-rays. Fig. 2 shows the experimental setup for the commercial coin battery (CR2023). The setup consists of a pinhole and a 2D X-ray detector system. The pinhole is made of Ta with a diameter of 0.5 mm and a thickness of 2 mm. The detector system consists of an image intensifier (II), an optical lens and a digital CCD camera with an efficiency of about 20% at 100 keV. The effective diameter of the X-ray entrance window is 4 inches. The effective area of the CCD camera is 1344 (horizontal) × 1023 (vertical) pixels, which is equivalent to 72 mm × 54 mm. The angle between the incident X-ray beams and the scattered X-ray direction at the center of the 2D X-ray detector is fixed at 90°. The pinhole and the X-ray detector are placed at 40 mm and 120 mm from the sample to measure an area of 20 mm × 20 mm inside the sample.

Two types of commercial batteries, CR2023 and CR123A, were measured. CR2023 is a coin battery with a diameter of 20 mm and a thickness of 3.2 mm, and CR123A is a cylindrical battery with a diameter of 17 mm and a height of 34.5 mm. The X-ray beam size was 0.025 mm or 0.05 mm in the vertical direction and 25 mm in the horizontal direction. The battery was set on a *XYZ* movable stage, and Compton-scattered

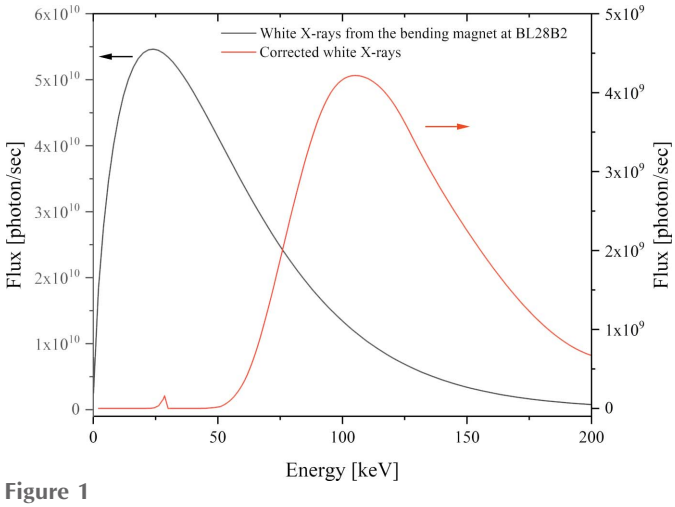

Figure 1
Photon flux as a function of energy at BL28B2 (black) and with absorption correction by Sn with 1 mm thickness (red).

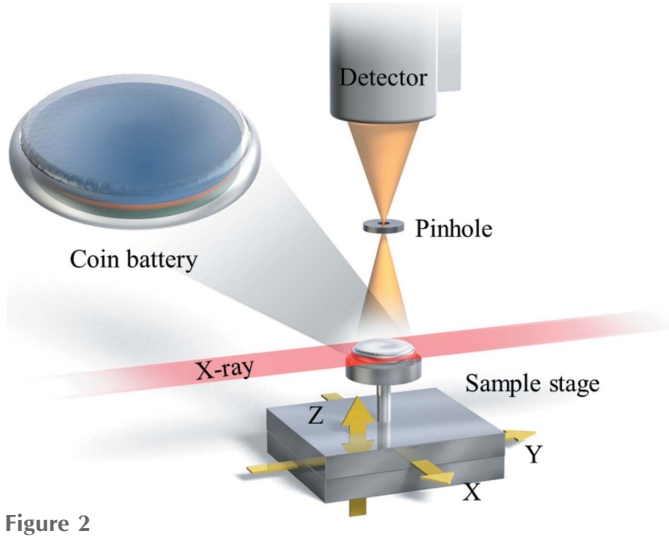

Figure 2
Compton scattering imaging setup for the measurement of a commercial coin battery (CR2023). The thicknesses of MnO_2 and Li in the CR2023 are 1.8 mm and 0.6 mm, respectively.

X-rays from the sample were measured by scanning the X-ray beams along the vertical (*Z*) direction. The probing volume is defined by the X-ray beam height and the area viewed by the pixels of the 2D X-ray detector through the pinhole.

3. Results and discussion

Figs. 3(*a*) and 3(*b*) show the in-plane cross-sectional images near the middle height of CR2023 with different modes: quick-scan and high-resolution. For the quick-scan mode, the exposure time is 34 ms and the height of the incident X-rays is 0.05 mm. The spatial resolution is 0.5 mm (*X*) × 0.5 mm (*Y*) × 0.05 mm (*Z*), which is dependent on the pinhole size and the vertical beam size. For high spatial resolution mode, the exposure time is 3 s and the height of the incident X-rays is 0.025 mm. The spatial resolution is 0.5 mm (*X*) × 0.5 mm (*Y*) × 0.025 mm (*Z*). The quick-scan image [Fig. 3(*a*)] shows clearly the internal structure near the spacer region, including the container case made of stainless steel (SUS) and the cathode made of MnO_2. In high spatial resolution mode [Fig. 2(*b*)], the horizontal lines of the spacer are also observed

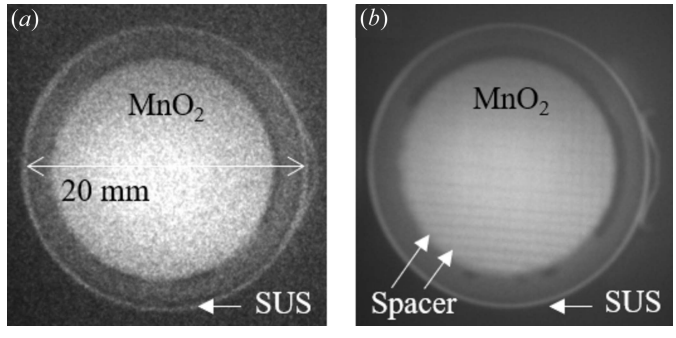

Figure 3
CSI of a coin battery at the spacer region. (*a*) Quick-scan imaging. (*b*) High spatial resolution imaging.

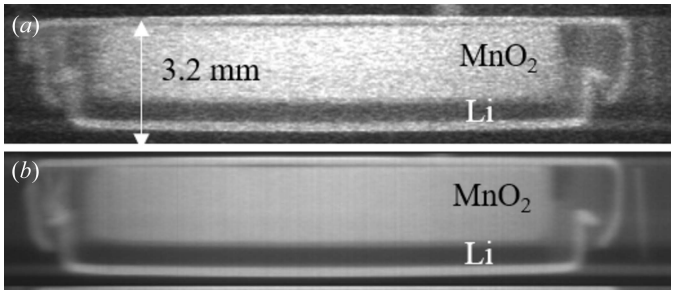

Figure 4
Cross-sectional imaging of the stacked CSIs at the center of the coin battery. (*a*) Quick-scan imaging. (*b*) High spatial resolution imaging.

due to higher spatial resolution along the *Z*-direction and longer exposure time.

The whole three-dimensional image of CR2023 was reconstructed by stacking in-plane cross-sectional images at different vertical (*Z*) positions, where 74 images were stacked for the quick-scan mode, and 148 images for the high spatial resolution mode. Figs. 4(*a*) and 4(*b*) show the vertical cross-sectional images of the 3D reconstructed images at the center of the battery for the quick-scan and high spatial resolution modes. In both images, the SUS case, the MnO_2 cathode, the Li anode and the separator are observed, although the Li anode and the separator are weak due to light elements and thinness.

Figs. 5(*a*) and 5(*b*) show the intensities of the reconstructed images along the *Z*-direction at the center of the battery. A step-like structure caused by the separator is clearly observed at the boundary between the anode and cathode. Compared with the air outside the SUS case, the region of the Li anode exhibits significant X-ray intensity, indicating that CSI is a useful technique to observe Li anodes. On the other hand, spike-like structures are observed at the outer side of the SUS case. This is probably due to increased incident X-ray intensity at the probing volume, caused by slight inclination of the surface of the SUS case. Overall, the present result reproduces

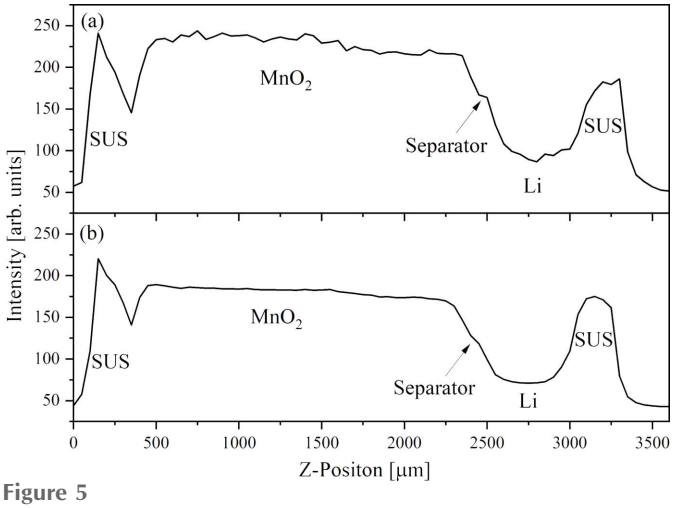

Figure 5
One-dimensional CSI along the *Z*-position at the center region of the coin battery. (*a*) Quick-scan imaging. (*b*) High spatial resolution imaging.

the previous one obtained by the point-by-point method (Itou *et al.*, 2015), indicating that the current plane-by-plane technique works well.

A cylindrical battery CR123A was measured to confirm the applicability of the plane-by-plane technique. Fig. 6(*a*) shows the cross-sectional image of CR123A at the rolled electrode region. The incident X-rays are 0.05 mm in height and 25 mm in width, and the exposure time was 3 s. The cylindrically rolled structure is clearly observed, although the separator is blurred due to the lack of spatial resolution with the 0.5 mm-diameter pinhole. Fig. 6(*b*) shows a vertical cross-section of the 3D image reconstructed by stacking 85 cross-sectional images near the positive pole. The total exposure time was 3 min. This result shows that the plane-by-plane technique is applicable to another type of battery.

As shown above, the internal structures of CR2023 and CR123A have been clearly observed by the plane-by-plane technique of Compton scattering imaging without any energy-discrimination of detected X-rays. The reason for this being that Compton scattering dominates the photon–electron interaction at such a high-energy X-ray region greater than 100 keV, resulting in substantially reduced elastic and fluorescence X-rays as the background.

Itou *et al.* (2015) reported that the Compton scattering intensity at the cathode (MnO_2) of the coin battery changed

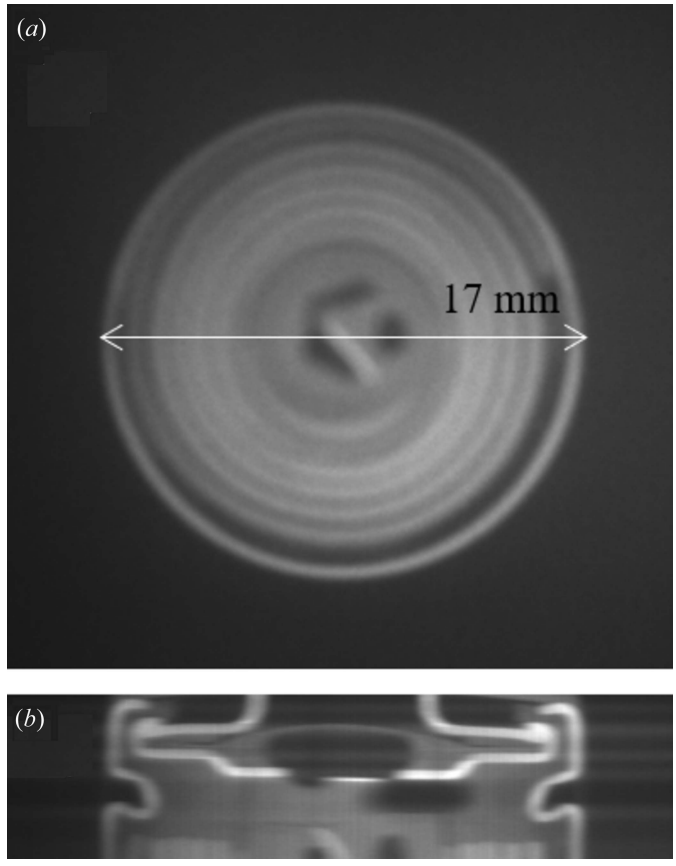

Figure 6
(*a*) CSI of the cylindrical battery at the cathode and anode region. (*b*) Cross-sectional image of the stacked CSIs around the positive electric pole.

by 5% during the discharging process. Since the CSI intensity at the MnO_2 region is almost constant, as shown in Fig. 4, the change of Compton scattering intensity is larger than the experimental noise. We expect that further CSI of Li ion batteries will reveal the changes in Li ion content during the charging and the discharging processes.

4. Summary

A CSI technique with the plane-by-plane geometry was applied to coin and cylindrical batteries. A cross-sectional image of the coin battery (CR2023) is directly obtained with an exposure time of 34 ms, and the three-dimensional image is reconstructed by stacking the cross-sectional images obtained at different vertical (Z) positions with a total time of 3 s without rotating the sample. The advantage of this technique is its applicability to electrochemical devices, such as batteries, under working conditions. The cross-sectional image can be directly obtained to visualize the dynamic behavior of the region of interest. In addition, this non-destructive imaging technique using high-energy X-rays can be applied to commercial products, structural materials, objects of cultural or archaeological significance and others.

Funding information

The experiment of CSI was performed with the approval of JASRI (grant Nos. 2015A2047, 2016A1330, 2018B1842, 2019B1700).

References

Boldo, E. M. & Appoloni, C. R. (2014). *Radiat. Phys. Chem.* **95**, 392–395.
Chikaura, Y., Iida, S., Kawado, S., Mizuno, K., Kimura, S., Matsui, J., Umeno, M., Ozaki, T., Shimura, T., Suzuki, Y., Izumi, K., Kawasaki, K., Kajiwara, K. & Ishikawa, T. (2001). *J. Phys. D Appl. Phys.* **34**, A158–A162.
Guzzardi, R. & Licitra, G. (1988). *CRC Crit. Rev. Bioeng.* **15**, 237–268.
Harding, G. & Harding, E. (2010). *Appl. Radiat. Isot.* **68**, 993–1005.
Itou, M., Orikasa, Y., Gogyo, Y., Suzuki, K., Sakurai, H., Uchimoto, Y. & Sakurai, Y. (2015). *J. Synchrotron Rad.* **22**, 161–164.
Margret, M., Menaka, M., Venkatraman, B. & Chandrasekaran, S. (2015). *Nucl. Instrum. Methods Phys. Res. B*, **343**, 77.
Sakurai, Y. (1998). *J. Synchrotron Rad.* **5**, 208–214.
Suzuki, K., Barbiellini, B., Orikasa, Y., Kaprzyk, S., Itou, M., Yamamoto, K., Wang, Y. J., Hafiz, H., Uchimoto, Y., Bansil, A., Sakurai, Y. & Sakurai, H. (2016). *J. Appl. Phys.* **119**, 025103.
Suzuki, K., Suzuki, A., Ishikawa, T., Itou, M., Yamashige, H., Orikasa, Y., Uchimoto, Y., Sakurai, Y. & Sakurai, H. (2017). *J. Synchrotron Rad.* **24**, 1006–1011.
Tanaka, T. & Kitamura, H. (2001). *J. Synchrotron Rad.* **8**, 1221–1228.